

# A simple model for some unusual properties of martensitic transformation

S. Sreekala<sup>1</sup>, Rajeev Ahluwalia<sup>2</sup>, and G. Ananthakrishna<sup>(1,3) \*</sup>

<sup>1</sup> *Materials Research Centre,*

*Indian Institute of Science, Bangalore-560012, India*

<sup>2</sup> *Theoretical Division, Los Alamos National Laboratory,  
Los Alamos, New Mexico 87545*

<sup>3</sup> *Centre for Condensed Matter Theory,  
Indian Institute of Science, Bangalore-560012, India*

We report a detailed numerical investigation of a recently introduced two dimensional model for square-to-rectangle martensitic transformation that explains several unusual features of the martensitic transformation. This model includes inertial effects, dissipation, long-range interaction between the transformed domains and an inhomogeneous stress field to describe the effect of lattice defects which serves as nucleation centers. Both single-site nucleation and multi-site nucleation has been studied for single quench situation and thermal cycling. The final stage morphologies of single-site nucleation and multi-site nucleation bear considerable similarity suggesting that the initial distribution of the defects is not important. Thermal cycling using continuous cooling and heating simulations show the existence of hysteresis in the transformation. More importantly, the rate of energy dissipated occurs in the forms of bursts with power law statistics for their amplitudes and durations which explains the results of acoustic emission signals observed in experiments. When the system is cycled repeatedly in a restricted domain of temperatures, the dissipated bursts of energy are repetitive, a feature observed in experiments. The associated morphology shows a complete reversal of the martensite domains thus throwing light on the mechanism underlying the shape memory effect. The model also exhibits tweed like patterns.

PACS numbers: 81.30.Kf, 05.40.-a, 64.60.Ht, 45.70.Ht

## I. INTRODUCTION

### A. Motivation

Martensitic transformation often exhibits unusual features that are not expected of a first order transition. One such effect is the well documented pretransitional effect observed as the system approaches the martensitic transformation temperature [1, 2, 3, 4]. The associated enhanced levels of fluctuation observed in several measurable quantities (such as the anomalous scattering and tweed structure) has been recorded in a number of different systems [1, 2, 3]. This feature, however, is the signature of critical fluctuations in a second order transition. As another example, consider an observation that relates to acoustic emission (AE), a feature that usually accompanies martensite transformation. Recently, in experiments on Cu-Al-Zn single crystals, Vives *et al* reported that the distributions of the amplitudes of the AE signals and their durations obey power law statistics when the samples were subjected to slow thermal cycling [5, 6] both during cooling and heating runs. The statistics were reported to be robust over a range of cooling and heating rates. Again, power law statistics imply scale free nature of the underlying process. However, in this case, as the AE signals are accumulated during thermal

cycling, there is no tuning as in second order transition. Thus, it is actually reminiscent of self-organized criticality introduced by Bak *et al* [8]. Another unusual and interesting property of the AE signals reported is the high degree of reproducibility and statistical correlation in time when the system is subjected to repeated thermal cycling over a restricted range of temperatures [9]. The near repetitive nature of AE signals during successive cycles have been shown to be correlated with the growth and shrinkage of martensite domains. Thus, exploring this correlated behavior should help us to understand the shape memory effect as well. Moreover, at a conceptual level, the nature of correlation of the repetitive AE signals is significantly different from the power law nature of the statistics observed during full thermal cycling mentioned above. Thus, it would be desirable to capture the seemingly conflicting properties using a single model. The purpose of the paper is to report a detailed study of a recently introduced two dimensional phenomenological model that is shown to explain both the power law statistics and correlated behavior of AE signals [10, 11]. As we shall show, the model also captures the precursor effect.

### B. Background

The martensitic transformations are technologically important class of first order, solid-solid, diffusionless structural phase transformations. Unlike other phase transformations where diffusion disperses the neighbour-

---

\*Electronic Mail: garani@mrc.iisc.ernet.in

ing atoms, here, neighbouring atoms in the parent phase remain so in the product phase also [12]. However, the lattice gets distorted due to spontaneous displacement of the atoms ( from their positions in the parent lattice) accompanying the discontinuous change in the shape and symmetry of the unit cell. This creates long-range strain fields which in turn strongly depend on the relative positions and orientations of the martensitic plates. (Typically, the martensite morphology consists of thin plate-like domains with twinned structure that are oriented along the elastically favorable habit plane directions.) Thus, the transformation path depends on continuously evolving configuration dependent long- range strain fields that eventually leaves the system in a metastable state. Thus, given a fixed quench, and hence a fixed amount of drive, the amount of transformed phase is fixed and further undercooling would be required to increase the product phase. For the same reason, the transformation occurs over a wide range of temperatures. On cooling, the transformation starts at a temperature  $M_s$ , called the martensite start temperature and is completed at a temperature  $M_f$  (martensite finish temperature). In the reverse heating cycle, the transformation is initiated at a temperature  $A_s$  (austenite start temperature ) and ends at a temperature  $A_f$  (austenite finish temperature), which in general can be much higher than the martensitic start temperature  $M_s$ . The related shape memory effect usually accompanies the transformation. The above features also imply that thermal fluctuations have little role in the transformation kinetics. Such martensites are called athermal. It must be mentioned that martensitic transformations can be induced by applying external stress. The combined use of temperature and stress have found many practical applications [13].

In athermal martensites, the martensitic phase nucleates from isolated regions in the crystal which are usually defects like dislocations or grain boundaries [14, 15, 16]. Thus, quenched disorder plays an important role in the initial kinetics of athermal martensites. Another interesting feature of these transformations is the autocatalytic cooperative nature of nucleation [14]. It is observed that a martensite domain that has nucleated from a specific site in the crystal, triggers the nucleation of other domains in the vicinity. Such a correlated nucleation was observed by Ferraglio and Mukherjee [14] who studied heterogeneous nucleation in Au-Cd alloys.

A large body of theoretical work has accumulated over the years [12, 16, 17]. ( See [18] for a recent summary of the status of theory.) Recent approaches use a continuum field theoretic models with strain or displacement fields as order parameters [19, 20, 21, 22]. Within this framework, Cao *et al* [21] have dealt with the problem of heterogeneous nucleation at localized defect sites by simulating the influence of defects through an inhomogeneous stress field. Recently, Wang and Khachaturyan [23] have investigated the dynamics of improper martensitic transformations based on a time dependent Ginzburg-Landau (TGDL) approach. This approach has also been

extended to proper martensitic transformation [24].

Here, we recall a few models relevant for the present work. The tweed structure has been explained as arising due to inhomogeneous distribution of the components of the martensitic alloy, for instance, Pd in Fe [22] using a strain based model. On the other hand, the power law behaviour of avalanches occurring in first order transitions has been modelled by using disorder based Ising models [25]. In this case, the power law statistics of avalanches arises in the presence of a critical amount of disorder. Since quenched-in-disorder (defects) plays an essential role in the nucleation process of martensitic transformation, it appears that these kinds of models [25] may be relevant to martensitic transformation. However, by subjecting the system to repeated hysteresis cycles, Vives *et al*, have verified that the system evolves towards a critical state independent of the initial treatment of the alloy suggesting a dynamical evolution of the system towards such a state. According to these authors [5], the interpretation is that in real martensites, although there are quenched-in defects, the disorder that is responsible for the power law is actually generated during the transformation itself. Indeed, this feature with lack of tuning is reminiscent of self-organized criticality, a word coined for slowly driven spatially extended systems evolving to a critical state where the statistics of avalanches obey a power law [8]. Since the introduction of this concept, there are large number of reports of physical systems exhibiting SOC like features, for example, earthquakes [26], acoustic emission from volcanic rocks [27], stress drops during the Portevin Le-Chatelier effect [28] and biological evolution [29], to name a few.

Recently, a simple two dimensional phenomenological model has been shown to capture the power law statistics under thermal cycling [10]. This model attempts to incorporate the essential features of systems evolving to SOC state, namely, slow driving, threshold dynamics, appropriate relaxational mode without any recourse to tuning any relevant parameter. Surprisingly, this model also captures the correlated nature of the AE signals when the system is cycled in a restricted range of temperatures [11], with the associated growth and decay of the martensite domains.

The purpose of this paper is to present the results of an extensive numerical simulations on this two dimensional model describing square-to-rectangle martensitic transformation [10, 11]. We discuss the results of a single-defect quench, multi-defect quench, thermal cycling over broad range of temperatures, the power law statistics arising in both in single and multi-defect cases, the correlated nature of AE signals and the associated shape memory effect, and finally the tweed like structure.

The organization of this paper is as follows. In section II, we describe our model starting from a free-energy functional and derive an equation of motion for a strain order parameter. The model has three free parameter one of which is the temperature. Section III contains the results of a detailed numerical simulations carried out for

various conditions of quench parameters. In section IV, we consider thermal cycling for single and multi-site cases both of which exhibit thermal hysteresis. By calculating the energy dissipated during the transformation, we show that the distribution of the amplitudes and durations of the energy bursts during thermal cycling obey power law statistics as in experiments [6]. Section V deals with the correlated behavior of AE signals and its correspondence with shape memory features. Section VI, deals with the tweed structure. We end the paper with some observations on the model.

## II. THE MODEL

The basic idea of the model is to include all the important features of athermal martentites such as inertial effects, long-range interaction and dissipation. The inertial effect is included by accounting for finite propagation time in a manner similar to that considered by Bales and Gooding [30, 32]. These authors have demonstrated that inertial effects prohibit the growth of martensite as a single variant in the presence of dissipation (in one dimension). Instead, the martensite grows as an alternating arrangement of the two variants. The reason for including dissipation stems from the recognition that the parent-product interface moves at near velocity of sound as suggested by the emission of AE signals. Associated with this movement, there is a dissipation which tends to relax the system towards local equilibrium. We include this through a Rayleigh dissipation functional [33]. (Note that conventional phase transformation take place at sufficiently slow pace thereby providing adequate time for quasi-steady state conditions to be attained in a short time.) We also include heterogenous nucleation at defect sites by including an appropriate strain energy [21].

In order to capture these seemingly different types of features within the scope of a single model, it is desirable to keep the model as simple as possible. To this end we first consider a 2d square-to-rectangle transition [19, 20]. However, the free energy in general depends on all the three strain components defined by

$$\begin{aligned} e_1 &= \frac{(\eta_{11} + \eta_{22})}{\sqrt{2}}, \\ e_2 &= \frac{(\eta_{11} - \eta_{22})}{\sqrt{2}}, \\ e_3 &= \eta_{12} = \eta_{21}, \end{aligned} \quad (1)$$

with

$$\eta_{ij} = \frac{1}{2} \left( \frac{\partial u_i}{\partial x_j} + \frac{\partial u_j}{\partial x_i} \right) \quad (2)$$

referring to the components of the linearized strain tensor and  $u_i$ 's are the displacement fields in the direction  $i$  ( $i = x, y$ ). The components  $e_1, e_2$  and  $e_3$  are the bulk dilational strain, deviatoric strain and shear strain respectively. The simplification we make is to assume that

it is adequate to consider the deviatoric strains to be the principal order parameter. This is a reasonable assumption considering the fact that volume changes are usually small. Henceforth, we denote the deviatoric strain by  $\epsilon(\vec{r})$  and define

$$\epsilon(\vec{r}) = \left( \frac{\partial u_x(\vec{r})}{\partial x} - \frac{\partial u_y(\vec{r})}{\partial y} \right) / \sqrt{2} = \epsilon_x(\vec{r}) - \epsilon_y(\vec{r}), \quad (3)$$

where  $u_x$  and  $u_y$  are respectively the displacement fields in the  $x$  and  $y$  directions.

The free-energy functional of our system with the order-parameter  $\epsilon$  is written as

$$F\{\epsilon(\vec{r})\} = F_L\{\epsilon(\vec{r})\} + F_{LR}\{\epsilon(\vec{r})\}, \quad (4)$$

where  $F_L$  is a local free-energy functional and  $F_{LR}$  is a nonlocal long-range term that describes transformation induced strain-strain interaction. In a scaled form, we write the local free-energy  $F_L$  as

$$F_L = \int d\vec{r} \left[ f_l(\epsilon(\vec{r})) + \frac{D}{2} (\nabla \epsilon(\vec{r}))^2 - \sigma(\vec{r}) \epsilon(\vec{r}) \right]. \quad (5)$$

where  $D$  and  $\sigma$  are in a scaled form. The latter represents the stress field due to localized defects in the crystal. (In a real crystal, lattice defects like dislocations and grain boundaries act as sources of stress concentration.) In the above equation,  $f_l(\epsilon(\vec{r}))$  is the usual Landau polynomial for a first order transition given by

$$f_l(\epsilon(\vec{r})) = \frac{\tau}{2} \epsilon(\vec{r})^2 - \epsilon(\vec{r})^4 + \frac{1}{2} \epsilon(\vec{r})^6. \quad (6)$$

Here,  $\tau = (T - T_c)/(T_0 - T_c)$  is the scaled temperature.  $T_0$  is the first-order transition temperature at which the free energy for the product and parent phases are equal, and  $T_c$  is the temperature below which there are only two degenerate global minima  $\epsilon = \pm \epsilon_M$ . The stress field  $\sigma(\vec{r})$  in Eqn. 5 modifies the free-energy  $f_l$  in such a way that the austenitic phase is locally unstable leading to the nucleation of the product phase.

The physical cause of the long-range interaction is the coherency in strain at the parent-product as well as the product-product interfaces. An effective long-range interaction between the deviatoric strains of the transformed domains has been shown to result from the elimination of the other strain components,  $e_1$  and  $e_3$ , using St. Venant compatibility constraint [22, 34]. Apart from determining the dependence on  $\vec{r}$ , one important feature is that such a kernel picks out the correct habit plane directions which in the present case are [11] and  $[1\bar{1}]$ . As one of our objectives is *to keep the model as simple as possible*, we have resorted to introducing a long-range kernel in a phenomenological way retaining the feature that allows the growth of martensitic domains along the habit plane directions [35]. (In the present case also, it is possible to use this approach to obtain the appropriate kernel). Wang and Khachatryan [23] have shown

that the interface can be described by accounting for coherency strains at the parent-product interface by including symmetry allowed fourth order anisotropic long-range interaction in the free energy, ie, a term which is invariant under  $\epsilon \rightarrow -\epsilon$ . We define the long-range interaction by

$$F_{LR}\{\epsilon\} = -\frac{1}{2} \int \int d\vec{r} d\vec{r}' G(\vec{r} - \vec{r}') \epsilon^2(\vec{r}) \epsilon^2(\vec{r}'). \quad (7)$$

As much as in the physical situation, in our model also, long-range interaction plays an important role in describing the growth of martensite domains. The kernel  $G(\vec{r} - \vec{r}')$  is best defined by considering the Fourier representation of the long-range term given by

$$F_{LR}\{\epsilon\} = \frac{1}{2} \int d\vec{k} B\left(\frac{\vec{k}}{k}\right) \{\epsilon^2(\vec{r})\}_k \{\epsilon^2(\vec{r})\}_{k^*}, \quad (8)$$

where  $\{\epsilon^2(\vec{r})\}_k$  is the Fourier transform of  $\epsilon^2(\vec{r})$  defined as

$$\{\epsilon^2(\vec{r})\}_k = \int \frac{d\vec{r}}{(2\pi)^2} \epsilon^2(\vec{r}) \exp(i\vec{k} \cdot \vec{r}). \quad (9)$$

The quantity  $\{\epsilon^2(\vec{r})\}_{k^*}$  is the complex conjugate of  $\{\epsilon^2(\vec{r})\}_k$ . The direction dependent kernel  $B(\vec{k}/k)$  contains information about the crystallographic details of the crystal and defines the habit plane. Apart from the favorable directions of growth of the product phase along  $[11]$  and  $[1\bar{1}]$ , the free-energy barriers should be large along the  $[10]$  and  $[01]$  directions. These features are well captured by the simple kernel

$$B\left(\frac{\vec{k}}{k}\right) = -\beta\theta(k - \Lambda) \hat{k}_x^2 \hat{k}_y^2, \quad (10)$$

where  $\hat{k}_x$  and  $\hat{k}_y$  are the unit vectors in  $x$  and  $y$  directions (The step function  $\theta(k - \Lambda)$  has been introduced to impose a cutoff on the range of the long-range interaction.) The constant  $\beta$  is the strength of the interaction. This kernel incorporates the effect of the interface in a simple way as the cost of growth progressively increases with the transformation in directions where the kernel is positive which not only aids growth along the habit plane directions but also limits the growth of domains transverse to it. We stress that this is only a simple choice and is not unique. Other kernels with similar orientation dependence will give similar results[35]. The real space picture of  $B(\vec{k}/k)$  is similar to the long-range interaction of Kartha *et al* [3].

Even though we have taken the deviatoric strain as the order parameter, basic variables are the displacement fields. Thus, we start with the Lagrangian  $L = T - F$ , where  $F$  is the total free-energy and  $T$  is the kinetic energy associated with the system. The kinetic energy is given by

$$T = \int d\vec{r} \rho \left[ \left( \frac{\partial u_x(\vec{r}, t)}{\partial t} \right)^2 + \left( \frac{\partial u_y(\vec{r}, t)}{\partial t} \right)^2 \right]. \quad (11)$$

Here  $\rho$  is the mass density. As mentioned in the introduction, since the parent-product interface moves rapidly, it is associated with a dissipation which we have represented by the Rayleigh dissipative functional [33]. Further, since deviatoric strains are the dominant ones, dissipative functional is written entirely in terms of  $\epsilon(\vec{r})$ ,

$$R = \frac{1}{2} \gamma \int d\vec{r} \left( \frac{\partial}{\partial t} \epsilon(\vec{r}, t) \right)^2. \quad (12)$$

(Here we have assumed that the bulk and shear strains equilibrate rapidly and hence do not contribute to the dissipation function.) Now consider the possibility of relating the above term to acoustic energy. As far as we know there are no attempts to capture the essential features of acoustic signals in the context of martensitic transformation. To model the AE signals, we recall that the mechanism of generation of the AE signals is generally attributed to the sudden release of the stored strain energy. One area where there has been some efforts to model AE signals is in plasticity. In this case, the production of AE signals is attributed to the abrupt motion of the dislocations. Consequently, the energy of AE signals,  $E_{ae}(r)$  is taken to be proportional  $\dot{\epsilon}^2(r)$ , where  $\dot{\epsilon}$  is the local plastic strain rate [36]. However, in general there is spatial inhomogeneity. Then the leading contribution to total energy  $E_{ae} \propto \int (\nabla \dot{\epsilon})^2 d^3r$ . This clearly has the same form as the Rayleigh dissipation functional [33] arising from the rapid movement of a localized region. Thus, while comparing results of the statistics of AE bursts, we need to simply compute  $R(t)$ .

We derive the equations of motion for  $\epsilon$  using the equations of motion for the displacement fields given by

$$\frac{d}{dt} \left( \frac{\delta L}{\delta \dot{u}_i} \right) - \frac{\delta L}{\delta u_i} = -\frac{\delta R}{\delta \dot{u}_i}, \quad i = x, y. \quad (13)$$

Using the above equation, after computing the functional derivatives, we get (see Appendix for details)

$$\rho \frac{\partial^2}{\partial t^2} \epsilon(\vec{r}, t) = \nabla^2 \left[ \frac{\delta F}{\delta \epsilon(\vec{r}, t)} + \gamma \frac{\partial}{\partial t} \epsilon(\vec{r}, t) \right], \quad (14)$$

which after scaling out  $\rho$  and  $D$  can be written in the form (in terms of rescaled space and time variables)

$$\begin{aligned} \frac{\partial^2}{\partial t^2} \epsilon(\vec{r}, t) = & \nabla^2 \left[ \frac{\partial f(\vec{r}, t)}{\partial \epsilon(\vec{r}, t)} - \sigma(\vec{r}) - \nabla^2 \epsilon(\vec{r}, t) + \gamma \frac{\partial}{\partial t} \epsilon(\vec{r}, t) \right. \\ & \left. + 2\epsilon(\vec{r}, t) \int d\vec{k} B(\vec{k}/k) \{\epsilon^2(\vec{k}, t)\}_k e^{i\vec{k} \cdot \vec{r}} \right], \quad (15) \end{aligned}$$

Here, both  $\beta$  and  $\gamma$  are to be taken as rescaled parameters. The structure of Eqn. (15) is similar to that derived in [30] for 1-d except for the long-range term. In the next section, we use the above equation to study the morphological evolution during martensitic transformations.

### III. NUMERICAL SIMULATIONS

We now describe the results of our numerical simulation for the morphological features. We discretize

Eqn.(15) on a  $N \times N$  grid using the Euler's scheme with periodic boundary conditions. The mesh size of the grid is  $\Delta x = 1$  and the smallest time step  $\Delta t = 0.002$ . Most results reported here correspond to  $N = 128, 256$ . However, wherever necessary, we have carried out simulations for higher  $N$ . A pseudo-spectral technique is employed to compute the long-range term [37]. In this method, we compute the discrete Fourier transforms of  $\epsilon^2(\vec{r}, t)$  and  $G(\vec{r})$ , take the product and then calculate the inverse Fourier transform. In all simulations reported in the paper, the cutoff  $\Lambda$  in the long-range expression defined in Eq.(10) is chosen to be 0.2. The inhomogeneous stress field  $\sigma(\vec{r})$  is appropriately chosen to describe the defect configuration (see below). We consider two situations corresponding to the nucleation at a single- defect site and at several defect sites.

### A. Nucleation at a Single-Defect Site

We begin with the study of nucleation and growth of domains under a single quench, starting from the austenite phase to the martensite phase. In general, the stress field due to several defects located at  $\vec{r}_j$  can be described by

$$\sigma(\vec{r}) = \sum_j^{j_{max}} \sigma_0(\vec{r}_j) \exp\left(\frac{-|\vec{r} - \vec{r}_j|^2}{\zeta_j^2}\right), \quad (16)$$

where  $\sigma_0(\vec{r}_j)$  is the magnitude of the stress field at sites  $\vec{r}_j$  which are randomly chosen defect sites,  $j_{max}$  is the total number of defect sites, and  $\zeta_j$  is the width of the field.

We first consider a single isotropic defect with its core located at the center of the system. Although, a single spherically symmetric defect is a rather artificial system, it is useful to clarify the physics of nucleation and growth in martensitic systems. For a single-defect case,  $\vec{r}_j = \vec{r}_0$ . We choose  $\zeta = 1$  and  $\sigma_0 = 0.3$ . With this value of  $\sigma_0$ , the system becomes locally unstable at the core  $\vec{r}_0$ . ( The threshold value of  $\sigma_0$  which makes the austenite phase unstable at that point is first determined and a slightly larger value is used. ) The parameters chosen for the simulations are  $\beta = 50$  and  $\gamma = 4$ . At  $t = 0$ , we start with  $\epsilon(\vec{r}, 0)$  distributed in the interval  $[-0.005, 0.005]$  representing the austenite phase and simultaneously 'turn on' the stress field  $\sigma(\vec{r})$  as we quench the system to  $\tau = -2.0$ .

Figure 1 shows the nucleation and growth of the martensite domains from the defect core at various instants of time. (Grey regions represent the austenite phase with  $\epsilon = 0$ , black and white regions represent the two variants of martensite characterized by  $\epsilon = \pm\epsilon_{eq}$ . ) We note here that the magnitude of strain in the two domains  $|\epsilon_{eq}|$  are larger than  $\epsilon_M$  ( obtained from Eq. (6)) due to the contribution arising from the long-range term. In a short time after quench ( $t \sim 7.5$ ), we observe the emergence of a small nucleus with  $\epsilon = \epsilon_{eq}$ . In addition, we also see the emergence of domains of the other

variant ( $\epsilon = -\epsilon_{eq}$ ) adjacent to the nucleus in the [11] and  $[1\bar{1}]$  directions. (We remark here that the mechanism of twinning in this model is the same as that discussed in [30, 32], i.e, kinetic energy minimization in the presence of dissipation.) The structure further develops into twinned arrays, propagating along [11] and  $[1\bar{1}]$  directions, as can be clearly seen in the snapshot at time  $t = 16.25$ . This snap shot also reveals an interesting feature namely the creation of nuclei ( $\epsilon = \epsilon_{eq}$ ) located close to the  $+x$  and  $-y$  directions, located at a finite distance from the propagating arrays. As the twinned fronts propagate, several additional nuclei are created at finite distances from the original propagating fronts as can be seen from the snap shot at  $t = 18.5$ . This can be attributed to the accumulation of long -range stress fields at these sites. These new nuclei give birth to secondary fronts that also propagate along [11] and  $[1\bar{1}]$ . These observations in our simulation are in accordance with the collective nucleation mechanism discussed in [23] and the experiments by Ferraglio and Mukherjee [14]. The propagation of these new secondary fronts continues till they 'collide' with the pre-existing martensite domains and stop ( $t = 20$ ). The morphological evolution eventually stops beyond  $t = 50$ .

Figure 2, shows the corresponding evolution of the area fraction  $\phi$  of the martensitic phase ( $\circ$ ). The area fraction is computed by counting the number of points on the grid for which  $|\epsilon(\vec{r}, t)| > 0.5$ . The transformation is seen to start around  $t \sim 15$ . The fraction increases sharply till about  $t \sim 20$ , beyond which it saturates to a value close to 0.31. The spurt in the growth between  $t = 15$  and 20 roughly coincides with the creation of the first set of additional nuclei.

### B. Nucleation at Several Defect Sites

Now we consider a more realistic case of several defect sites where the nucleation can occur. Here, we assume a random distribution of defects. In the present simulation, we choose  $j_{max} = 16$  (nearly 0.1% of the total number of sites and  $N = 128$ ) and consider  $\sigma_0(\vec{r}_j)$  to be uniformly distributed in the interval  $[-0.3, 0.3]$ . All other parameters are same as that for the single-defect case. Initially, the system is in a homogeneous state with  $\epsilon(\vec{r}, 0)$  uniformly distributed in the interval  $[-0.005, 0.005]$ . At  $t = 0$ , we turn on the stress-field  $\sigma(\vec{r})$ . In Fig. 3, we show the evolution of the system at specifically chosen instants of time. As in the case of single- site nucleation, around  $t = 15$ , nucleation of the product phase is seen to occur at several sites. By  $t = 17.5$ , these nuclei grow into twinned lenticular shape. Several additional nuclei emerge at finite distance from these original domains. These new sites at which the product phase nucleates most often coincides with the pre-existing defect sites. However, occasionally, nucleation does occur at sites where there were no defects due to stress accumulation arising from the long-range term, as in the case

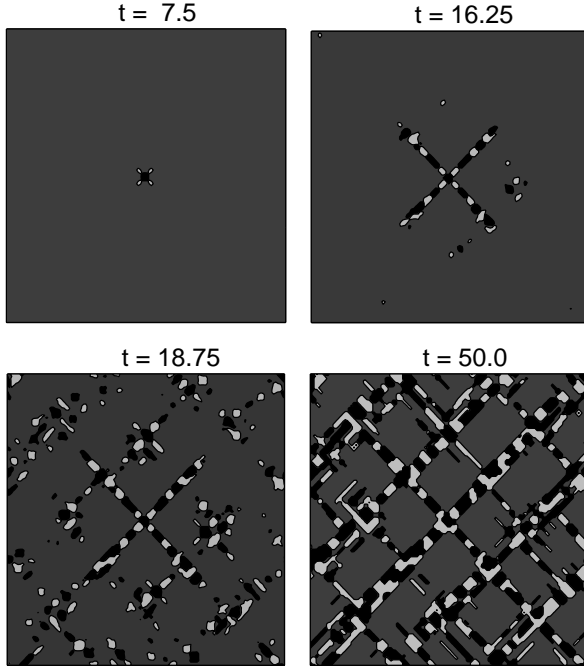


FIG. 1: Morphological evolution for nucleation at a single-defect with  $\beta = 50$ ,  $\gamma = 4$  and  $\tau = -2.0$ . Grey cells correspond to the austenite phase and the black and the white to the two martensite variants.

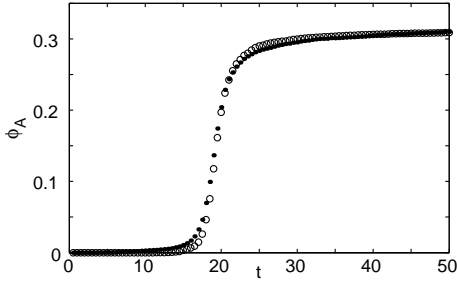


FIG. 2: Plot of the transformed area fraction  $\phi_A$  with respect to time for  $N=128$ ,  $\beta = 50$ ,  $\gamma = 4$ , and  $\tau = -2.0$ . ○ correspond to single-site case and ● corresponds to the multi-site defect case.

of single-site nucleation. As can be seen from the snapshot at  $t = 15$ , there is a rapid growth of the product phase along  $[11]$  and  $[\bar{1}\bar{1}]$  directions forming a criss-cross pattern of the martensite domains. We find that there is very little growth beyond  $t = 25$  and by  $t = 50$  the growth practically stops. A comparison of this final configuration with the corresponding single-site nucleation shows that the final morphologies are very similar implying that the morphology evolution is independent of the original defect ( stress-field) configuration. As for the morphology, we can see thin needle-like structures emerging from larger domains. Figure 2 also shows the time evolution of the area fraction  $\phi$  for multi-defect case (●) which is very similar to the single-defect case, which

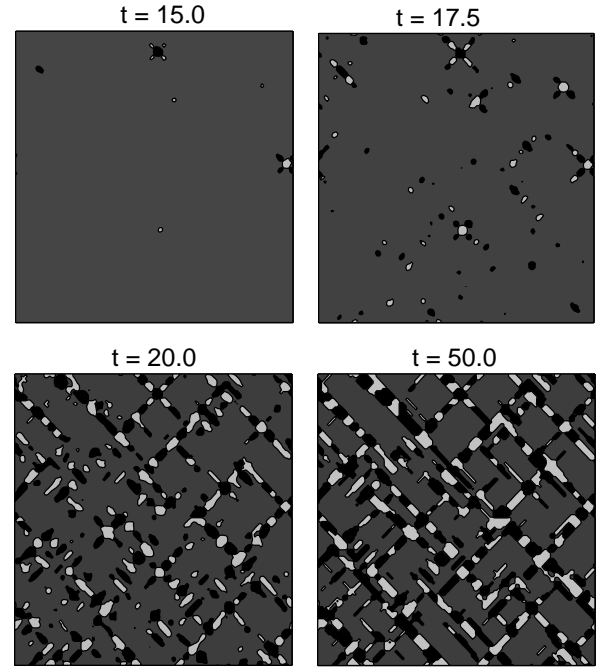


FIG. 3: Morphological evolution for multi-defect case with defect density 0.1% for  $\beta = 50$ ,  $\gamma = 4$  and  $\tau = -2.0$

again emphasizes the fact that the time evolution is not sensitive to initial defect configuration. All the adaptive domain adjustments take place beyond this time regime. Thereafter, the area fraction saturates.

We briefly remark on the influence of the two parameters  $\beta$  and  $\gamma$  on the morphology. The quantity  $\gamma$  represents the strength of dissipation and  $\beta$  the strength of the transformation induced long-range interaction. We find that the lateral width of the arms for smaller  $\beta$  is larger than that corresponding to larger values of  $\beta$  for a fixed value of  $\gamma$ . The area fraction is higher for smaller  $\beta$  which can be attributed to the fact that a lower value of  $\beta$  corresponds to a lower interaction between the transformed regions and hence, lower energy cost to grow transverse to the direction of propagation. ( Note that  $\beta = 0$  corresponds to symmetric growth.) Now consider the influence of the dissipative term on the morphology. Our finding is that the twin width is larger for larger values of  $\gamma$ . This result can be understood by noting that the overdamped case ( $\gamma \gg 1$ ) corresponds to growth as a single variant [30]. With the inertial effects, growth as a single variant is prohibited by high kinetic energy cost. In view of this, for large values of  $\gamma$ , the dissipative term dominates and the system grows as a single variant for a larger distance than that for the low damping case.

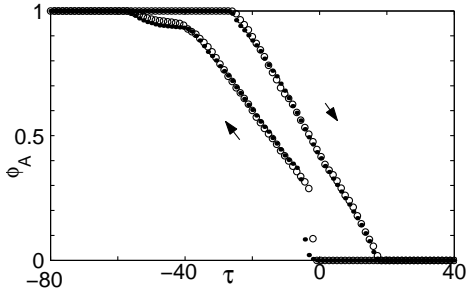


FIG. 4: Area fraction of the transformed phase  $\phi_A$  as a function of  $\tau$  for both single defect ( $\circ$ ) and multi-defect ( $\bullet$ ) nucleation cases. The parameter values are  $\beta = 50, \gamma = 4$  and  $N = 128$ . The defect density in multi-defect is 0.1% of sites.

#### IV. THERMAL CYCLING AND HYSTERESIS

##### A. Morphological Features

One key feature of a martensitic transformation is the hysteresis observed when the system is subjected to thermal cycling. Here, the system is cooled at a specific rate from the high temperature phase to the low temperature phase and then subsequently heated back to the high temperature phase. We have performed ‘continuous cooling’ and ‘heating’ computer simulations where we change  $\tau$  at a constant rate: the interval  $\tau = 40$  to  $-80$  is cooled in 1000 time steps. We have monitored both the morphology and the area fraction of the transformed phase for single-defect nucleation as well as multi-defect nucleation case with several system sizes ( $N=128, 256$ ). We use the same initial conditions for both these cases as that used for a single quench situation. The initial condition for the reverse transformation is the final configuration obtained during the cooling run.

In Fig. 4, we have shown the variation of the area fraction  $\phi_A$  with  $\tau$  for the heating and the cooling runs for the single defect case ( $\bullet$ ) and multi defect case ( $\circ$ ) for  $N = 128$ . In the cooling run, for the multi-defect case, the transformation starts around  $\tau \sim -2.0$  showing a rapid increase in  $\phi_A$  ( $\sim 30\%$ ). Thereafter, there is a nearly linear increase up to 90% at which the growth rate tapers off. The system gets fully transformed at  $\tau_{mf} \sim -60$ . In the heating run, the reverse transformation does not start till  $\tau_{as} \sim -22.0$  and thereafter,  $\phi_A$  decreases almost linearly till the transformation is nearly complete around  $\tau \sim 18$ . As can be seen from the figure (Fig. 4), the difference between the hysteresis cycles corresponding to the multi- site defect nucleation and single-defect nucleation cases is small.

We have followed the morphological evolution of the martensitic domains both for the single and multi-defect cases. Here, we shall only discuss the more realistic multi-defect case. Figure 5 shows the snap shots of the pattern at specifically chosen values of  $\tau$  as the system is taken through a cycle. In the snapshot corresponding

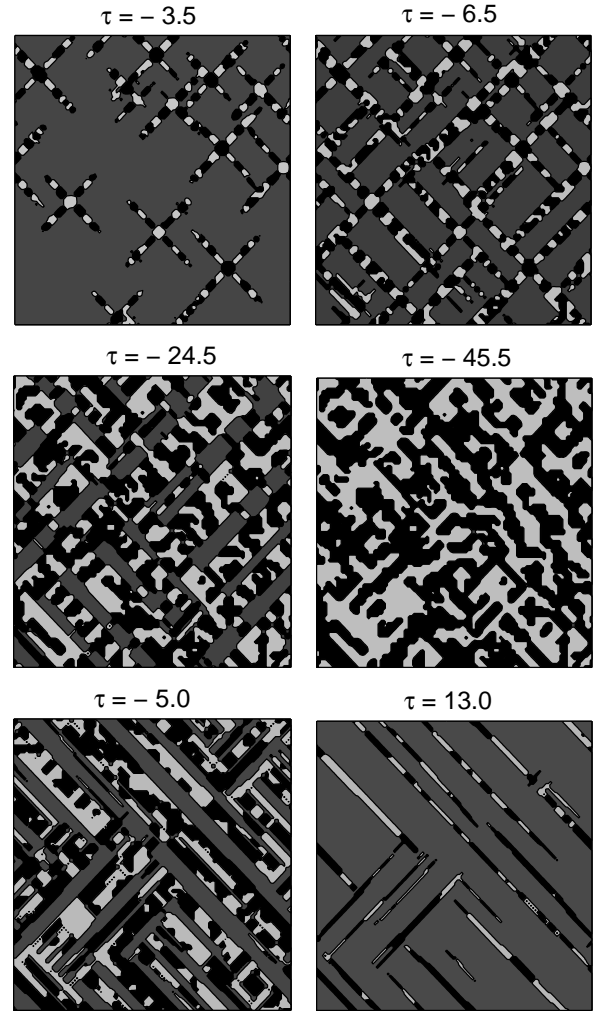


FIG. 5: Morphological evolution during a cooling and heating cycle. The parameter values are  $\beta = 50, \gamma = 4$  and  $N = 128$  with a defect density 0.1% of the sites.

to  $\tau = -3.5$ , one can see the nucleation of martensitic domains at multiple locations. As the system is further ‘undercooled’ to lower values of  $\tau$ , not only does these twins propagate in the  $[11]$  and  $[1\bar{1}]$  directions, the thickness of the martensite domains also increases. This can be seen from the snapshots corresponding to  $\tau = -6.5$  and  $\tau = -24.5$ . As the system is further undercooled, the twin width further increases with the last regions transforming around  $\tau = -59$ . A late stage snap shot at  $\tau = -45.5$  corresponding to  $\phi \sim 90\%$  is shown. For the heating cycle, the final configuration of the cooling run is taken as the initial configuration. The austenite phase appears around  $\tau \sim -22$ . As  $\tau$  is further increased, the martensite phase can be seen to be gradually disappear in the snapshots corresponding to  $\tau = -5$  and 13. Further, one can see that the overall morphology in the final stages of the heating run is significantly different from the initial stages of the cooling run. Thus, in our model, there is no long term memory effects, though there is

short term memory as will be shown later. Finally, by  $\tau = 18.0$ , the martensite phase disappears completely.

### B. Power Law Statistics During Thermal Cycling

From Fig. 4, it appears that changes in  $\phi_A$  are smooth on the scale shown in the figure. In reality, on a finer scale, the changes in  $\phi_A$  are actually jerky. In fact, in experiments, thermal cycling is accompanied by the emission of acoustic energy in the form of bursts, a feature that reflects the jerky nature of the transformation. In the model, as mentioned earlier, the energy of acoustic signals is captured by the rate of energy dissipated given by  $R(t) = -dE/dt$ . We have calculated  $R(t)$  during the heating and cooling runs. Figure 6 shows  $R(t)$  as a function of  $\tau$  with the inset showing the enlarged section of the peak. The figure clearly shows that the rate of energy release occurs in bursts consistent with acoustic emission studies [5] during thermal cycling.

Since, in experiments one finds that the AE signals show a power law statistics, we have investigated the distributions of the amplitudes of the AE signals and their durations. Denoting the amplitude of  $R(t)$  by  $R_A$ , we find that the distribution  $D(R_A)$  of  $R_A$  has a tendency to approach a power law, i.e.,  $D(R_A) \sim A^{-\alpha_R}$  with an exponent  $\alpha_R$ . Figure 7 shows a log-log plot of  $D(R_A)$  as a function of  $R_A$ , for both the single-site nucleation case ( $\bullet$ ) and the multi-defect case ( $\circ$ ). From the figure, it is clear that both these cases exhibit the same exponent value  $\alpha_R \sim 2.5$  over three orders in  $D(R_A)$ . In experiments, one also finds that duration of these bursts also obey a power law statistics. To verify this, we have also plotted the distribution  $D(\Delta t)$  of the durations  $\Delta t$  of energy bursts for both the single and multi defect cases. We find that  $D(\Delta t) \sim \Delta t^{-\tau_R}$  with an exponent value  $\tau_R \approx 3.2$ , although, the scaling regime is not as impressive as for  $R_A$ . (Here, we remark that typically the scaling regime for the durations of the events is much smaller than that for the amplitudes even in models of SOC [8, 38].) We have also calculated the conditional average  $\langle R_A \rangle_c$  for a given value of  $\Delta t$  [31]. This is expected to obey a power law given by  $\langle R_A \rangle_c \sim \Delta t^{x_R}$ . The value we get is about  $x \approx 1.36$  for both these single and multi defect nucleation cases. Using these values, we find that the scaling relation  $\alpha = x(\beta - 1) + 1$  is satisfied quite well. We have also carried out a similar analysis on  $R(t)$  for the heating run. Even though, the changes in  $R(t)$  occurs in bursts, we find the scatter is considerably more than for the cooling run. We will comment on this aspect later.

A comment is in order regarding the exponents. In experiments one actually plots the distribution for the amplitude of the AE signals, while in our model acoustic energy plays a natural role. Thus, while comparing the exponents values, one needs to use  $R_A \sim A_{AE}^2$ , where  $A_{AE}$  is the amplitude of the AE signal. Using the relation between the two joint probability distributions  $D(R_A, \Delta t) \propto D(A_{AE}, \Delta t)/A_{AE}$ , one easily finds

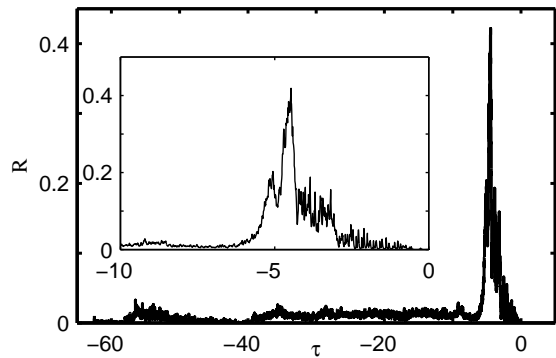


FIG. 6:  $R(\tau)$  as a function of  $\tau$  with inset showing enlarged section of the peak during cooling. The parameter values are  $\beta = 50, \gamma = 4$  and  $N = 256$ . The defect density in multi-defect is 1% of sites.

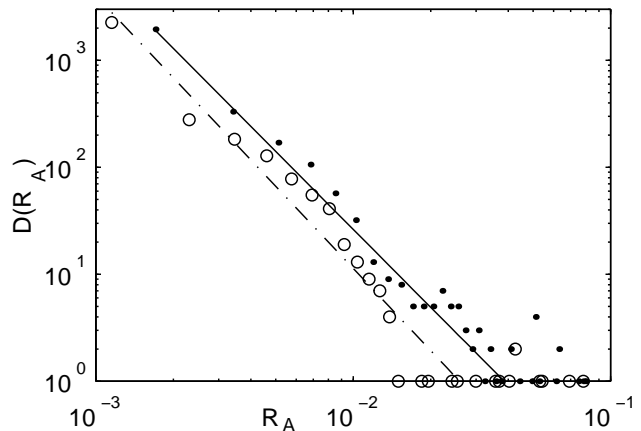


FIG. 7: log-log plot of  $D(R_A)$  as a function of  $R_A$ . The parameter values are  $\beta = 50, \gamma = 4$  and  $N = 256$ . The defect density in multi-defect is 1% of sites. [ $\circ$  corresponds to single-defect case and  $\bullet$  corresponds to multi-defect case.]

that  $\alpha_R = (\alpha_{AE} + 1)/2$  with the other two exponent values remaining unchanged. Using the experimental values [5] of  $\alpha_{AE} \approx 3.8$ , ( $\tau_{AE} \sim 3.8$  and  $x_{AE} \sim 1$ ), we see that the calculated value of  $\alpha_R \approx 2.4$ . Considering the fact that our model is two dimensional, we see that the agreement of the exponent values is reasonable. Here, it should be pointed out that even the number of martensite variants in 3-D are more than in 2-D. Thus, it would be unrealistic to expect that the mechanisms in 3-D can be accounted for in 2-D.

We now explain the origin of the power law statistics in the model. This can be traced to the fact that we have included important ingredients of SOC dynamics, namely, the threshold dynamics, dissipation, the generation of large number of metastable states during the transformation, and a relaxation mechanism for the stored energy. The relaxation of the stored energy occurs at very fast time scales comparable to time scale of the speed of



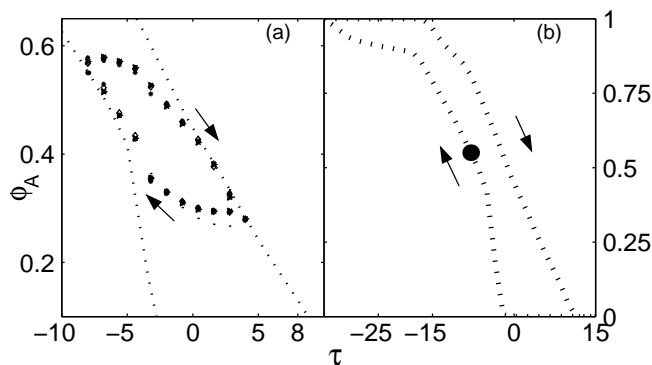


FIG. 8: (a).Area fraction  $\phi$  during thermal cycling in the interval  $\tau = -8$  to 4 for cycles 1 ( $\circ$ ), 2 ( $\Delta$ ), 3 ( $\bullet$ ), 4 ( $\triangleright$ ). (b)Hysteresis for the full cycle from the austenite to the martensite phase and back. ( $\bullet$ ) is the starting point of the small thermal cycles.

sound as can be seen from the fact that the basic variables are the displacement fields. ( We note that this is the fastest time scale.) Indeed, from our simulations we find that the interface movement occurs at time scales of a few units of (scaled) time as can be inferred by rapid increase in the area fraction of the transformed phase, typically of the order of a few units of scaled time. (See Fig. 2.) Compared to this the driving force generated by thermal cycling increases with temperature slowly which is one of the characteristic features of SOC dynamics.

Another important feature of the model, as also that of SOC dynamics, is the creation of large number metastable states during cooling or heating runs. This is a direct consequence of an interplay between the local free energy ( free energy barrier) and the long-range interaction between the transformed domains as can be seen from the following reasoning. We note that the value of the long-range term at any spatial location is the result of the superposition of the contributions arising from the spatial distribution of the already transformed domains. As a consequence, the free energy surface at any given time is a complex terrain of local barriers ( metastable states). It must be noted that these local thresholds are *self generated* ( transformation induced). At a given time, these local thresholds must be overcome by the increase in the driving force arising from the slow cooling (or heating). We note that once a local barrier is overcome, part of the driving force goes in creating a new twin and the rest is dissipated in the form of burst of energy due to the advancing one or more interfaces. The fact that long-range interaction is at the root of creating the local thresholds is *further supported by the fact that we find a power law distributions even in the single- site nucleation case*. (See  $\bullet$  in Fig. 7.) The presence of defect sites only serves to trigger the initial nucleation process. This must be contrasted with disorder based Ising models[25] which also produce power law statistics for avalanches and field induced hysteresis. However, as mentioned earlier, Vives

*et al* have verified that in martensite transformation, it is the dynamical disorder ( transformation induced) that is at the root of the avalanches. This exactly what is well captured by the present model.

## V. SHAPE MEMORY EFFECT

### A. Correlated behavior of AE signals

As mentioned in the introduction, one experimental result (known for some time) is the highly correlated behavior of AE signals when the system is subjected to thermal cycling in a small temperature interval. To verify if this result can be captured by our model, consider the system being cooled from the austenite phase to a point in the martensite phase where a desired amount of martensite phase has developed. Starting from an appropriate point ( shown as  $\bullet$  in Fig. 8b, here chosen to be  $\phi \sim 0.58$  in the full thermal cycle), we subject the system to repeated thermal cycling in a small temperature range  $\tau_{min} = -8$  and  $\tau_{max} = 4$ . As in the case of full thermal cycling, for the small heating cycle also, the final configuration attained at  $\tau_{max} = 4$ , is taken as the initial configuration for the cooling run. Calculations have been performed for a range of parameter values of  $50 \leq \beta \leq 10$  and  $5 \leq \gamma \leq 1$ . For the present calculation, we have used  $\beta = 35$  and  $\gamma = 4$ . The value of  $\beta$  used here is higher than that reported in our earlier paper [11]. We shall discuss the influence of increasing  $\beta$  soon. Other parameter values are  $\Lambda = 0.2$ ,  $\zeta = 1$  and  $N = 128$ . During the first few cycles, the loops in the area fraction  $\phi$  verses  $\tau$  drift slightly, but stabilize after a first few cycles, here, after the sixth cycle. The first few cycles play the role of the *training* period known in experiments. After these first few cycles the system eventually circulates in the same set of configurations as we will show. ( The number of training cycles in the model is only few, however in experiments, the training period is typically a few cycles for *CuAlZn* [9], but could be much larger in some other alloys.)

During the training cycles, the energy dissipated  $R(t)$  evolves continuously, stabilizing only after the training period. A plot of  $R(t)$  for several forward and reverse cycles ( seventh to tenth ) after stabilization is shown in Fig. 9. It is clear that the energy bursts (which mimic the AE signals), as in experiments [39, 40], exhibit a near repetitive pattern in time (temperature) during successive heating and cooling parts of the cycles. As can be seen the bursts are much more noisy when compared to slightly smaller value of  $\beta$  used in our earlier study[11]. Further, we find that increasing  $\beta$  requires more cycles to stabilize ( for instance, the cycles stabilize after the fourth for  $\beta = 25$ ).

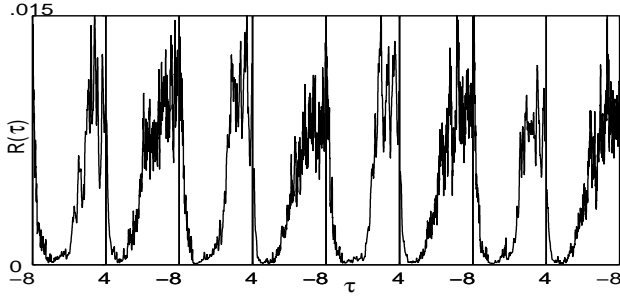


FIG. 9: Repetitive nature of  $R(\tau)$  for cycles 7 to 10.

### B. Connection to shape memory effect

In order to establish a correspondence between  $R(t)$  and the changes in the spatial configuration of the martensite domains, we have simultaneously monitored the morphology over all the cycles. We find that the morphology changes drastically during the first few cycles even though the macroscopic state of system in terms of  $\phi - \tau$  returns to nearly the same point at the end of each cycle. The domain configurations at the beginning of first few cycles are shown in Fig. 10. Figure 10 a is the starting morphology for the first cycle that has been obtained by slowly cooling from the austenite phase. Figure 10d is that obtained at the end of sixth cycle. As can be seen, most changes occur during the first few cycles with large number of changes occurring in the first cycle itself. We find that during the first cycle itself, most of the curved twin interfaces in the initial configuration (Fig. 10a) are rendered straight and several small twins coalesce to form a single variant of the same type. One can also notice that some regions of the austenite phase separating the martensite domains are washed out. Subsequent cycles also have the same effect, but less effective. The morphology stabilizes even though some curved interfaces with small regions of martensite phases remain (see the top left edge in Fig. 10d). After the sixth cycles very little changes could be detected.

Now consider the changes in the morphology during a single cycle in the region where  $R(t)$  is repetitive. The snapshots of the morphology during one such stabilized cooling and heating cycle, the seventh one, (starting from the initial configuration shown in Fig. 10d) at selected intervals is displayed in Fig. 11. It is clear that during heating, the martensite domains shrink, opening up the austenite phase and some martensite domains even disappear. However, during cooling these domains reappear and the eventual morphology at the end of the cycle is practically recovered on returning to the starting point on the  $(\phi, \tau)$  diagram. As can be seen, the final configuration obtained during the seventh cycle, Fig. 11 d can be seen to be practically the same as Fig. 10 d which is the initial configuration for the seventh cycle. These observations are consistent with that observed in experiments [9].

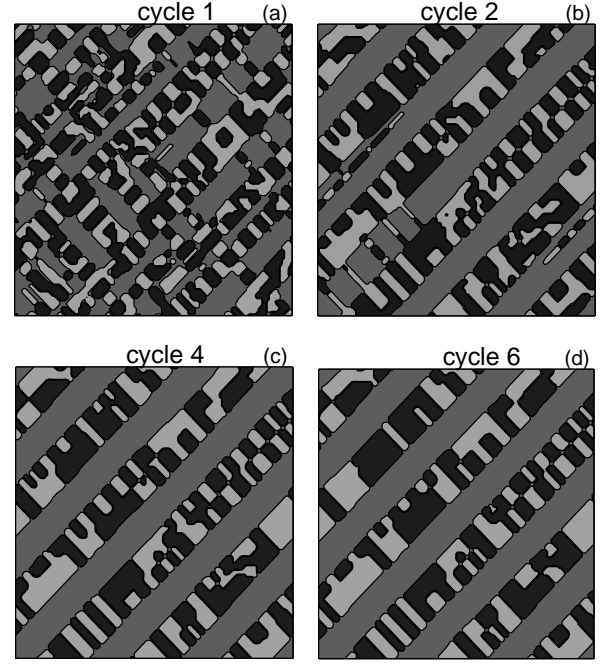


FIG. 10: Morphology of the initial configurations at  $\tau = -8.0$  for the first, second, fourth and the sixth thermal cycles.

Now, we attempt to provide a physical explanation for the repetitive nature of the energy bursts and the reversal of the morphology under thermal cycling. To understand this, we need to understand the role played by the training cycles. Indeed, the repetitive pattern of the energy bursts during successive cycles (after the training period) is an indication that the system traverses through the same set of metastable states. From Fig. 10a, we note that the initial configuration for the first cycle has a large number of small domains compared to the configuration obtained after the sixth cycle shown in Fig. 10 d. In addition, the twin interfaces of Fig. 10a are rough. (The interface is considerably more curved for small  $\beta$  values. Compare Fig. 3 of Ref. [11]. For the present case, it is relatively straight.) Such configurations are generally expected to have higher energy compared to straighter ones. Thus, the initial configuration used for cycling (Fig. 10a) corresponds *only* to a local shallow minimum. During the first few cycles, the free energy landscape is so modified that it smoothen's out the energy barriers corresponding to large number of twin interfaces in Fig. 10a) with very little change in the area fraction. As in the case of power law distribution, a crucial role in smoothening process is actually played by the long-range interaction term, as the growth (shrinkage) of a martensite domain is influenced by the configuration of rest of the domains. To verify this, we have computed the free energy  $F_{LR}$  arising from the long-range interaction between the domains and find that it actually becomes more negative with successive cycles saturating after first few cycles. This additional contribution leads to a reduction in the local free energy,

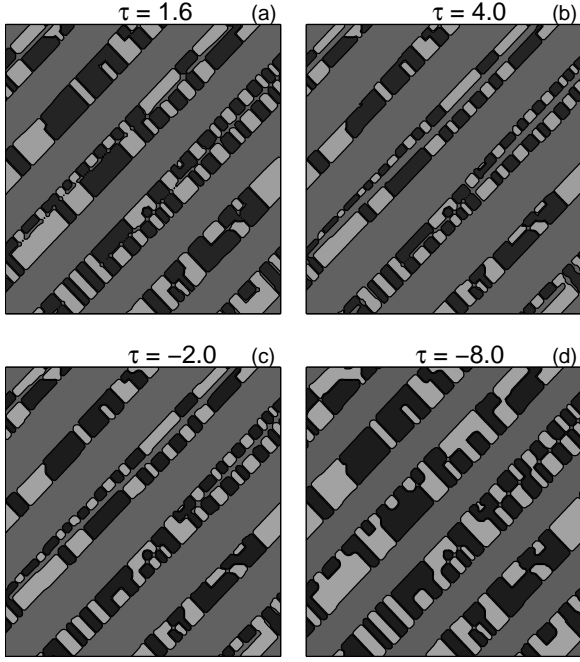


FIG. 11: Sequential morphological snapshots for  $\tau = 1.6(a)$ ,  $4.0(b)$ ,  $-2.0(c)$ ,  $-8.0(d)$  during the seventh cycle. The initial configuration for the cycle is that shown in Fig.10(d).

$F_L$ , as well. The net effect is to create a deeper set of metastable states for the system to circulate for the stabilized cycles. Within one such stabilized cycles, say seventh, the starting configuration (Fig. 10d) has the lowest free energy reaching a maximum at the end of a heating cycle, i.e., at  $\tau = 4.0$ , Fig. 11b. Thereafter it decreases during cooling. Note that the morphology at  $\tau = 4.0$  is significantly different from the starting morphology. The increasing or decreasing width of the martensite domains as we decrease or increase the temperature is surprisingly similar to that observed in experiments. ( See Fig. 12 of Ref.[9].)

## VI. PRETRANSITIONAL EFFECTS

Now we consider the possibility of recovering pretransitional effects in our model. As mentioned in the introduction, the mechanism attributed by Kartha *et al* is the dependence of the elastic constant on local disorder in composition. It is clear that once the basic mechanism is included, the model should lead to results similar to that in Kartha *et al*. We shall adopt the same idea and assume that the transition temperature depends on local compositional fluctuations through

$$T_0(\vec{r}) = T_0(\bar{c}) - A\delta c(\vec{r}), \quad (17)$$

where  $A$  is the relative strength of coupling to compositional fluctuations  $\delta c$ , assumed here to be randomly distributed. In scaled variable that we use, this leads to  $\tau$

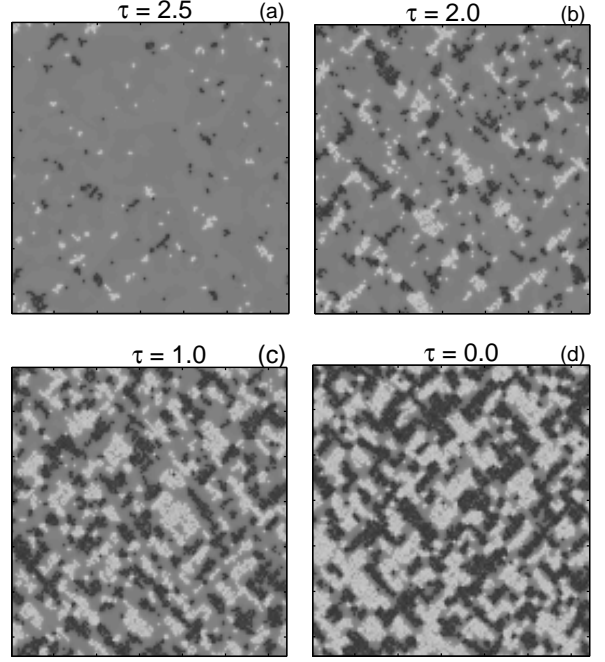


FIG. 12: Development of Tweed like pattern

being replaced by  $\tau = \tau(\bar{c}) + a\delta c$ , where  $\bar{c}$  is the average concentration and  $a$  is a scaled variable.

In our simulations, we assume that the initial concentration fluctuations, considered as frozen, are drawn from a normalized Gaussian. In our case, we just need to solve the equations of motion numerically for various values of  $\tau$  and  $a$ . (We have varied  $a$  from 0.0 to 1.2.) The range of values of  $\beta$  and  $\gamma$  wherein we find the tweed structure is in the region of relatively low values. ( $\beta < 20$  and  $\gamma < 0.7$ .) Here, we report results for  $a = 0.9$ ,  $\beta = 10$  and  $\gamma = 0.1$ . A typical set of morphologies are shown in Fig. 12. The pretransitional effects become noticeable even when  $\tau = 4$ . For  $\tau = 2$  the directionality of the tweed pattern is already evident. As we decrease the temperature, this structure becomes more dominant. It must be mentioned here that in our case, these patterns do not change after reaching a steady state. Thus, we do not have the dynamic tweed structure reported by Kartha *et al*. This is because, in our model the effect of temperature goes only in the local free energy and there are no thermal fluctuations. We also note that the pretransitional effects are pronounced when both  $\beta$  and  $\gamma$  are small. We shall comment on this later. However, we note that including the changes in the transition temperature on local disorder is somewhat similar to the contribution from defects except that internal stresses ( arising from deviations from the average concentration) are of much smaller magnitude compared to that due to defects. Thus, it is clear that one can mimic the present situation through Eq. 16 by appropriate choice of  $\sigma_0$  and  $\zeta_i$ . In our case, the  $a - \tau$  plane, the boundary between the austenite and the tweed phases is linear in the range

(0,0) to (1.2,4).

## VII. SUMMARY AND DISCUSSIONS

In summary, we have presented the results of a comprehensive study of the dynamics of strain driven martensitic transformations within the framework of a two dimensional square-to-rectangle transition. Due to the fact that the long-range term is introduced phenomenologically, the model should be viewed as a model whose primary aim is to capture the essential physics of the transformations. We however note that it includes all the important contributions arising from different mechanisms in a transparent way. In doing so, we are able to study the dynamics of the strain driven transition that explains the three unusual features of the martensitic transformation that were sought to modelled. The first important feature that emerges from the model is the fact that the elastic energy stored is released in the form of bursts. (Note that we have also established a correspondence between the dissipative functional and the energy of AE signals.)

Second, the model provides a proper basis to explain the power law statistics of the AE signals observed in experiments. As stated earlier, the power law statistics arises due to the fact that we have included threshold dynamics, dissipation, the generation of large number of metastable states during the transformation, and a relaxation mechanism for the stored energy whose time scale is much faster than the time scale of the drive force. It is interesting to point out that both cases of single-defect and multi-defect nucleation lead to power laws strongly suggesting that quenched defects do not play any role in the power law. The model also predicts the near repetitive bursts of energy under successive thermal cycles in a small temperature interval as observed in experiments on acoustic emission [9, 39, 40]. This comes as a surprise as the nature of correlation in the latter case is 'periodic' in contrast to the scale free nature of correlations discussed in the power law statistics of AE signals. More importantly, these bursts of energy have been shown to be correlated to the growth and shrinkage of martensite plates. The underlying cause of the correlated nature of AE signals and reversal of the morphology during successive cycles after the training cycles has been traced to the influence of the long-range interaction term. The role of training cycles is also elucidated. During the training period the long-range term has a tendency to smoothen out higher energy barriers in the free energy landscape. This in turn induces a transformation pathway along a unique set of *low energy metastable configurations*. We expect that our analysis provides a good insight into the shape memory effect which finds immense applications in a variety of areas from mechanical actuators to bio-medical applications [42]. To the best of authors knowledge, this is the first model which shows near full reversal of morphology under thermal cycling. Finally, it is not surprising that the model also reproduces tweed like fea-

tures.

A comment may be in order on the physical interpretation of the cause of the memory effect in our model. Recall that during the course of the transformation (either in single quench situation or in thermal cycling), nucleation occurs at sites that are not necessarily the sites of quenched defects, but arising from constructive superposition of long- range stress fields of the preexisting domains. However, as quenched defects have been represented by a Gaussian stress profile in our model, in the same spirit, these new nucleation sites could in principle be interpreted as creating new defects at these sites. (See the comment in Ref. [41].) We also believe that it may be possible to model this with an additional degree of freedom for the defect kinetics. We expect that our analysis provides a good insight into the shape memory effect which finds immense applications in a variety of areas from mechanical actuators to bio-medical applications [42].

It is interesting to note the similarity of morphological patterns with real micrographs. Patterns studied in the context of single-defect and multi-defect nucleation show that the eventual morphology are independent of the the original defect configuration. It is not clear if this is true of real systems although experiments of Vives *et al* [5] provide an indirect evidence. In addition, the model shows hysteresis under thermal cycling. Even though, the model explains several generic features stated above, we stress that our model is not material specific.

As mentioned the pretransitional effect is pronounced when both  $\beta$  and  $\gamma$  values are small. The low values of  $\gamma$  is physically understandable as one expects that there would be hardly any dissipation in the high temperature phase where there are no martensite domains. The smallness of  $\beta$  is also understandable physically (as the magnitude of fluctuations in the composition is not high). However, the value of  $\beta$  cannot be determined in terms of the elastic constants as in the case where the kernel is derived by using the compatibility relation [3].

Some comments may be in order on SOC type of features obtained in the model. We note here that unlike most SOC models where noise is essential [8, 38], the model is fully dynamical in the sense that noise has no role in the generation of power law statistics. In spirit, the model is closer to that by Gil and Sornette[43] where an explicit threshold term is introduced in the form of a subcritical Hopf bifurcation. However, it must be pointed out that noise is essential in their model as well. Lastly, to the best of the authors knowledge, this is one of the few fully continuous space-time dynamical (noise free) model for SOC.

## Acknowledgments

Part of this work was carried out when one of the authors (RA) was supported by JNCASR which is gratefully acknowledged.

## APPENDIX

Here we present some details of the derivation of Eqn. 15. To start with we evaluate  $\frac{\delta F_L}{\delta u_x}$ ,

$$\frac{\delta F_L}{\delta u_x} = \int d\vec{r} \left[ \left( \frac{\partial f}{\partial \epsilon(\vec{r})} - \sigma(\vec{r}) \right) \frac{\delta \epsilon(\vec{r})}{\delta u_x(\vec{r})} + D(\nabla \epsilon) \frac{\delta \nabla \epsilon(\vec{r})}{\delta u_x(\vec{r})} \right], \quad (\text{A.1})$$

Using the definition for  $\epsilon$ , the above expression reduces to a compact form

$$\frac{\delta F_L}{\delta u_x} = \frac{\partial}{\partial x} \left[ - \left( \frac{\partial f}{\partial \epsilon(\vec{r})} - \sigma(\vec{r}) \right) + D \nabla^2 \epsilon(\vec{r}) \right] = - \frac{\partial}{\partial x} \left[ \frac{\delta F_L}{\delta \epsilon(\vec{r})} \right]. \quad (\text{A.2})$$

An analogous calculation for  $\frac{\delta F_L}{\delta u_y}$  holds except for a negative sign on the left hand side with interchange of the  $x$  with  $y$ . Similarly, one can show that

$$\frac{\delta F_{LR}}{\delta u_x} = \frac{\partial}{\partial x} \left[ \epsilon(\vec{r}) \int d\vec{r}' G(\vec{r} - \vec{r}') \epsilon^2(\vec{r}') \right] = - \frac{\partial}{\partial x} \left[ \frac{\delta F_{LR}}{\delta \epsilon(\vec{r})} \right] \quad (\text{A.3})$$

and a similar equation for  $u_y$ . The functional derivative ( $x$  component) for the dissipation functional is

$$\frac{\delta R}{\delta \dot{u}_x} = -\gamma \frac{\partial}{\partial x} \left( \frac{\partial}{\partial t} \epsilon(\vec{r}, t) \right), \quad (\text{A.4})$$

and a similar equation for  $\dot{u}_y$ . One also finds

$$\frac{d}{dt} \left( \frac{\delta L}{\delta \dot{u}_i} \right) = \rho \frac{\partial^2}{\partial t^2} u_i(\vec{r}, t), i = x, y. \quad (\text{A.5})$$

Then, using these results in Eq.(13), and taking appropriate derivatives with respect  $x$  and  $y$ , we get the equation for the strain order parameter as

$$\begin{aligned} \rho \frac{\partial^2}{\partial t^2} \epsilon(\vec{r}, t) = & \nabla^2 \left[ \frac{\partial f(\vec{r}, t)}{\partial \epsilon(\vec{r}, t)} - \epsilon(\vec{r}, t) \int d\vec{r}' G(\vec{r} - \vec{r}') \epsilon^2(\vec{r}', t) \right. \\ & \left. - \sigma(\vec{r}) - D \nabla^2 \epsilon(\vec{r}, t) + \gamma \frac{\partial}{\partial t} \epsilon(\vec{r}, t) \right]. \end{aligned} \quad (\text{A.6})$$

Using  $F = F_L + F_{NL}$ , in a compact form the above equation can be written as

$$\rho \frac{\partial^2}{\partial t^2} \epsilon(\vec{r}, t) = \nabla^2 \left[ \frac{\delta F}{\delta \epsilon(\vec{r}, t)} + \gamma \frac{\partial}{\partial t} \epsilon(\vec{r}, t) \right]. \quad (\text{A.7})$$

- 
- [1] S. Muto, S. Takeda, R. Oshima, and F. E. Fujita, J. Phys.: Condens. Matter **1**, 9971 (1989).
  - [2] I.M. Robertson and C. M. Wayman, Phil. Mag A, **48**, 421 (1983); *ibid* **48**, 443 (1983); *ibid* **48**, 629 (1983).
  - [3] Sivan Kartha, J. A. Krumhansl, J. P. Sethna, and L. K. Wickham, Phys. Rev. B **52**, 803 (1995).
  - [4] R. Oshima, M. Sugiyama and F. E. Fujita, Metall. Trans A, **19A**, 803 (1988).
  - [5] E. Vives, J. Ortin, L. Manosa, I. Rafols, R. Perez-Margane and A. Planes, Phys. Rev. Lett. **72**, 1694 (1994).
  - [6] E. Vives, I. Raflos, L. Manosa, J. Ortin and A. Planes, Phys. Rev. B **52**, 12644(1995); See also, Ll. Carrillo *et al*, Phys. Rev. Lett. **81**, 1889 (1998).
  - [7] A. Planes, J. L. Macqueron, M. Marin, G. Guenin and L. Dalaey, J. Phys. (Paris), **C4**, 615 (1982); A. Amengual, Ll. Manosa, F. Marco, C. Picornell, C. Segui and V. Torra, Thermochemica Acta, **111**, 195 (1987).
  - [8] P. Bak, C. Tang, and K. Wiesenfeld, Phys. Rev. A **38** 364 (1988);
  - [9] F. C. Lovey and V. Torra, Prog. Mater. Sci. **44**, 189 (1999).
  - [10] R. Ahluwalia and G. Ananthakrishna, Phys. Rev. Lett. **86**, 4076 (2001).
  - [11] S. Sreekala and G. Ananthakrishna, Phys. Rev. Lett. **90**, 135501-1 (2003).
  - [12] See J. W. Christian, G. B. Olson, and M. Cohen, J. de Physique **C 8**, 3 (1995); P. C. Clapp, J. de Physique **C 8**, 11 (1995); G. B. Olson, Mater. Sci. and Engineering **A273-275**, 11 (1999).
  - [13] R.E. Newnham, MRS Bull., **18**, 24 (1993).
  - [14] P. L. Ferraglio and K. Mukherjee, Acta Metall **22**, 835(1974).
  - [15] J. W. Brooks, M. H. Loretto and R. E. Smallmann, Acta Metall. **27**, 1829 (1979).
  - [16] A. G. Khachaturyan, *Theory of Structural Transformations in Solids* (Wiley, New York).
  - [17] A. L. Roitbutd and G. V. Kurdjmov, Materials Science and Engineering, **39** 141 (1979).
  - [18] G. B. Olson, Mater. Sci. and Engineering **A273-275**, 11(1999).
  - [19] A. E. Jacobs, Phys. Rev. B **31**, 5984 (1985).
  - [20] J. A. Krumhansl, Solid State Commun. **84**, 251(1992).
  - [21] W. Cao, J. A. Krumhansl and R. J. Gooding, Phys. Rev. B **41**, 11319 (1990).
  - [22] S. Kartha, T. Castan, J. A. Krumhansl and J. P. Sethna, Phys. Rev. Lett. **67**, 3630 (1991)
  - [23] Y. Wang and A.G. Khachaturyan, Acta Mater. **45**, 759(1997).
  - [24] A. Artemev, Y. Jin and A.G. Khachaturyan, Acta mater. **49**, 1165 (2001); Y.M. Jin, A. Artemev and A.G. Khachaturyan, Acta mater. **49**, 2309 (2001); A. Artemev, Y. Wang and A.G. Khachaturyan, Acta mater, **48**, 2503 (2000).
  - [25] J. P. Sethna *et al*, Phys. Rev. Lett. **70** 3347 (1993); E. Vives and A. Planes, Phys. Rev. B **50**, 3839 (1994); A. Magni, Phys. Rev. B **59**, 985 (1999).
  - [26] C. F. Richter, Ann. Geophys. **9**, 1 (1956).
  - [27] P. Diodati, F. Marchesoni and S. Piazza, Phys. Rev. Lett. **67**, 2239 (1990).
  - [28] G. Ananthakrishna, S. J. Noronha, C. Fressengeas and L. P. Kubin, Phys. Rev. E **60**, 5455 (1999).
  - [29] P. Bak and K. Sneppen, Phys. Rev. Lett., **71** 408 (1993).
  - [30] G. S. Bales and R. J. Gooding, Phys. Rev. Lett. **67**, 3412(1991).

- [31] I. Rafols and E. Vives, Phys. Rev. B **52**, 12651 (1995).
- [32] A. C. E. Reid and R. J. Gooding, Phys. Rev. B **50**, 3588(1994).
- [33] L. D. Landau and E. M. Lifschitz, *Theory of Elasticity*, 3rd ed.(Pergamon, Oxford, 1986).
- [34] S. R. Shenoy, T. Lookman, A. Saxena and A. R. Bishop, Phys. Rev. B **60**, R12537 (1999).
- [35] This choice is not unique. Further, it may be possible to derive an appropriate kernel which couples bilinear terms in  $\epsilon(r)$  and  $\epsilon(r')$ . However, we expect that the functional form of  $B(\vec{k}/k)$  would be complicated.
- [36] J. Weiss, F. Lahaie, and J. R. Grasso, J. Geo. Research, **105**, 433 (2000).
- [37] C. Sagui and R. C. Desai, Phys. Rev. E, **49**, 2225 (1994).
- [38] H. J. Jensen, *Self - Organized Criticality*, (Cambridge University Press, Cambridge, 1998).
- [39] A. Amengual *et al.*, Thermochem. Acta **116**, 195 (1987).
- [40] C. Picornell *et al.*, Thermochem. Acta **113**, 171 (1987).
- [41] F.J. Perez-Reche *et al.*, Phys. Rev. Lett. **87**, 195701 (2001).
- [42] J. Van Humbeeck, M. Chandrasekharan, and L. Delaey, Endeavour, New Series, **15**, 148 (1991).
- [43] L. Gil and D. Sornette, Phys. Rev. Lett., **76**, 3991 (1996).